Fast Magnetic Domain-Wall Motion in a Ring-Shaped Nanowire Driven by a Voltage

Jia-Mian Hu,[*,†] Tiannan Yang,[†] Kasra Momeni,[†] Xiaoxing Cheng,[†] Lei Chen,[†] Shiming Lei,[†] Shujun Zhang,[†] Susan Trolier-McKinstry,[†] Venkatraman Gopalan,[†] Gregory P. Carman,[‡] Ce-Wen Nan,[§] and Long-Qing Chen[*,†]

[†]Department of Materials Science and Engineering, Pennsylvania State University, University Park, Pennsylvania 16802, United States

[‡]Department of Mechanical and Aerospace Engineering, University of California, Los Angeles, California 90095, United States

[§]School of Materials Science and Engineering, and State Key Lab of New Ceramics and Fine Processing, Tsinghua University, Beijing 100084, China

S Supporting Information

ABSTRACT: Magnetic domain-wall motion driven by a voltage dissipates much less heat than by a current, but none of the existing reports have achieved speeds exceeding 100 m/s. Here phase-field and finite-element simulations were combined to study the dynamics of strain-mediated voltage-driven magnetic domain-wall motion in curved nanowires. Using a ring-shaped, rough-edged magnetic nanowire on top of a piezoelectric disk, we demonstrate a fast voltage-driven magnetic domain-wall motion with average velocity up to 550 m/s, which is comparable to current-driven wall velocity. An analytical theory is derived to describe the strain dependence of average magnetic domain-wall velocity. Moreover, one 180° domain-wall cycle around the ring dissipates an ultrasmall amount of heat, as small as 0.2 fJ, approximately 3 orders of magnitude smaller than those in current-driven cases. These findings suggest a new route toward developing high-speed, low-power-dissipation domain-wall spintronics.

KEYWORDS: Magnetic domain-walls, fast motion, piezoelectrics, low-power spintronics, phase-field modeling
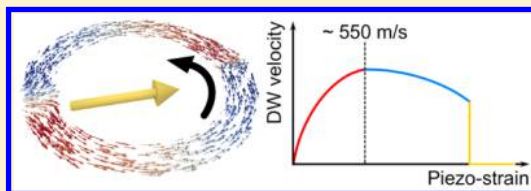
Unidirectional magnetic domain-wall motion in curved nanowires underpins new device concepts for logic,[1] sensors,[2] and memories.[3] Efficient low-power-dissipation domain-wall motion is the key to high-speed operation and miniaturization of these domain-wall-based devices. However, faster magnetic domain-wall motion typically requires larger driving electric current densities (via magnetic fields[4−6] or spin-torques[7−12]), which are relatively inefficient and dissipate substantial amounts of heat. This poses significant problems for controlling domain-wall motion on a small scale if electric current remains the main driving stimulus.

A much more desirable option is to use voltage rather than current to drive unidirectional magnetic domain-wall motion. However, this is challenging since voltages, unlike currents, do not induce unidirectional force fields on the domain-walls (e.g., the Ampère field, or effective field from spin-torques). Accordingly, voltage-driven magnetic domain-wall motion is typically oscillatory and bidirectional,[13] leading to relatively low average wall velocity (below 100 m/s). For the same reason, most existing reports[14−23] utilized voltage merely to manipulate the magnetic anisotropy to modify the energy barrier for domain-wall motion. For instance, by interfacing a magnet with a gate dielectric[14−19] (or ferroelectric[20−23]) layer, an applied voltage can modulate the magnetic interface anisotropy via electrostatic control of spin-polarized electrons[14−18,20,21] and/or ionic migration,[19] or modulate magnetoelastic anisotropy via the transfer of piezostrains.[22,23]

Here we show, upon applying static piezostrains to a ring-shaped magnetic nanowire (through applying static voltage to the piezoelectric disk underneath), magnetic domain-walls can propagate deterministically to the strain axis, but in an oscillatory manner. By changing the orientation of the piezostrains (through applying dynamic voltages) before magnetic domain-walls propagate back, a unidirectional magnetic domain-wall motion with an average velocity up to 550 m/s is demonstrated. This is comparable to current-driven magnetic domain-wall motion[11,12] and spin wave velocities. We also develop an analytical model to predict the dynamics of such strain-mediated voltage-driven unidirectional magnetic domain-wall motion. Furthermore, the analyses predict an ultralow heat dissipation (∼0.2 fJ) per 180° domain-wall circuit, along with ultralow energy consumption (∼4 fJ).

Results. Figure 1a shows the geometry of the proposed magnetic-piezoelectric nanostructure. A ring-shaped amorphous $Co_{40}Fe_{40}B_{20}$ (CoFeB) layer with both moderate magnetoelastic coupling[24] and low magnetic damping[25] (i.e., with low heat dissipation during magnetic domain-wall motion) is the representative nanomagnet. The dimensions are 300 nm (inner diameter) × 400 nm (outer diameter) × 5 nm (thickness). Phase-field simulations (see Methods) indicate

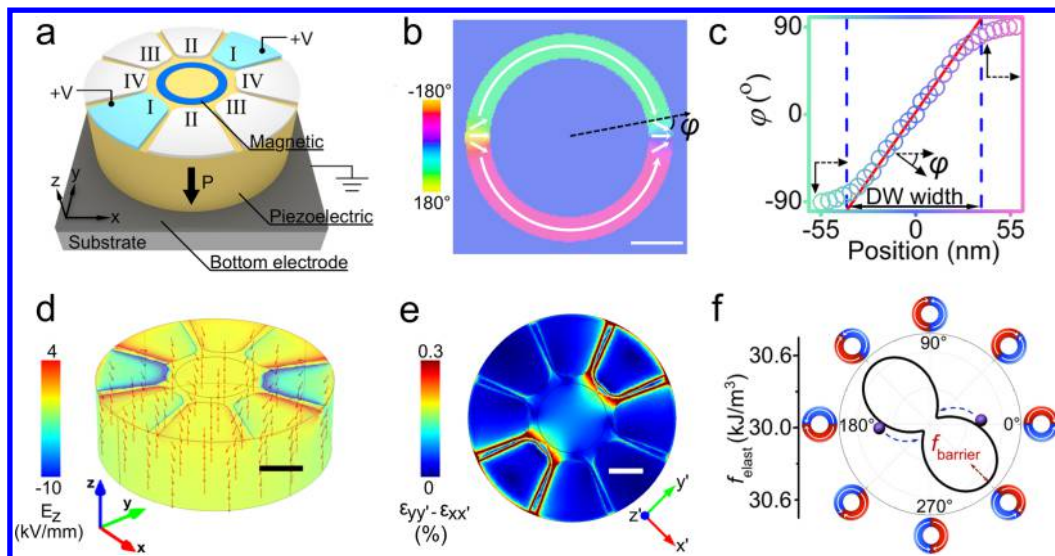**Figure 1.** (a) Schematics showing an amorphous $Co_{40}Fe_{40}B_{20}$ ring with a dimension of 300 nm (inner diameter) × 400 nm (outer diameter) × 5 nm (thickness) attached to a polycrystalline PZT disk of 1200 nm (diameter) × 400 nm (thickness) grown on a substrate and electrodes for applying out-of-plane electric fields. Identical positive electric voltages (+V) are applied to the top electrodes I−I, the bottom electrode is grounded at 0 V, and the other inactive top electrodes are kept under open-circuit condition. The remanent polarization (P) of PZT is along the −z direction. (b) Distribution of orientation angle φ in the ring (scale bar = 100 nm). (c) Profile of φ across one in-plane transverse domain-wall. The domain-wall width is given by the two cross points between the tangent line and the horizontal axes. Distributions of (d) electric fields and (e) biaxial in-plane piezostrain difference $\varepsilon_p = \varepsilon_{y'y'} - \varepsilon_{x'x'}$ in the PZT (scale bar = 200 nm) when applying a static voltage of 1.1 V to electrodes I−I. The small red arrows indicate the orientation of local electric fields. (f) Polar plot of elastic energy densities in magnetic rings whose two transverse domain-walls align along different orientations within the plane (see the surrounding schematics), on applying 1.1 V to electrodes I−I. Corresponding to the ring shown in b, the two domain-walls are initially at 0° and 180° as indicated by the spheres and tend to rotate to the energy minima at 45° and 225° (the axis of ε_p), respectively, as indicated by the dashed arrows.

that the rough-edged, amorphous CoFeB ring exhibits an onion-type domain structure[26] with two head-to-head transverse domain-walls of about 78 nm in width (Figure 1b and c) following the application/removal of a saturating static magnetic field along the +x direction. A cylindrically shaped disk of polycrystalline $Pb(Zr,Ti)O_3$ (PZT) is the piezoelectric material. The piezoelectric disk has a size of 1200 nm (diameter) × 400 nm (thickness) and is prepoled downward along the −z direction. The bottom electrode is electrically grounded. In this case, applying positive electric potential on any one of the four pairs of top 20 nm-thick Ti/Au electrodes (I−I, II−II, III−III, and IV−IV in Figure 1a) induces localized biaxial in-plane anisotropic piezostrains on the surface based on inhomogeneous surface electric field distributions and the clamped boundaries.[27] These surface piezostrains are then transferred to the CoFeB ring to drive the magnetic domain-walls.

For illustration, Figure 1d shows the three-dimensional electric-field distributions in the PZT disk calculated via finite-element simulations (see Methods) upon applying a static voltage of 1.1 V through electrodes I−I and keeping the other top electrodes under open-circuit condition. Only the bottom electrode (dark gray layer in Figure 1a) is grounded at 0 V. As shown by the arrows, the electric fields are pointing downward (i.e., parallel to the polarization). The background color suggests that electric fields concentrate around the bottom surfaces of the top electrodes (mostly on the edges of the active electrodes I−I), but the magnitude of these concentrated electric fields is well below the dielectric breakdown field of polycrystalline PZT (∼25 kV/mm, ref 28). Moreover, the simulated surface distribution of biaxial in-plane piezostrain difference ($\varepsilon_p = \varepsilon_{y'y'} - \varepsilon_{x'x'}$) is fairly uniform in the CoFeB ring

area (i.e., marked by the solid circle in Figure 1e) and with an average of about 0.0766%. The predicted strains are transferred to the CoFeB ring with negligible loss. This assumption is valid because the PZT disk is substantially thicker and wider than the CoFeB ring. The simulated equilibrium nonuniform strain distribution (see Supplementary Figure S1) predicts an average strain of about 0.0536% in the CoFeB. The reduction from 0.0766% is mainly attributed to shear lag effects near the edges.[29] Nonetheless, this strain is more than sufficient to drive a fast magnetic domain-wall motion as described below.

Figure 1f compares the elastic energy density in different CoFeB rings whose two magnetic domain-walls are located at different angles within the plane (see the surrounding schematics), when a uniform piezostrain of 0.0766% from the PZT is applied along the 45°/225° axis. These results were calculated from the phase-field model. As shown, the elastic energy density shows minima when both magnetic domain-walls are collinear to the axis of piezostrain. Therefore, in a CoFeB ring whose domain-walls are initially at 0° and 180° (represented by the spheres), the domain-walls would propagate to the energy minima at 45° and 225° (see the dashed arrows), respectively. Such strain-driven 45° magnetic domain-wall rotation is deterministic due to the presence of the energy density barrier (denoted as $f_{barrier}$ in Figure 1f) and has been experimentally demonstrated by the recent observation of the static magnetization distribution in a polycrystalline Ni ring of a micron-sized outer diameter grown on top of <011>-oriented $Pb(Mg_{1/3}Nb_{2/3})_{0.66}Ti_{0.34}O_3$ (PMN−PT) substrates.[30]

Figure 2a shows the changes in the instantaneous magnetic domain-wall velocities upon applying the static 1.1 V to the electrodes I−I (the top panel), calculated from the phase-field model. From the bottom panel of Figure 2a, it can be seen that
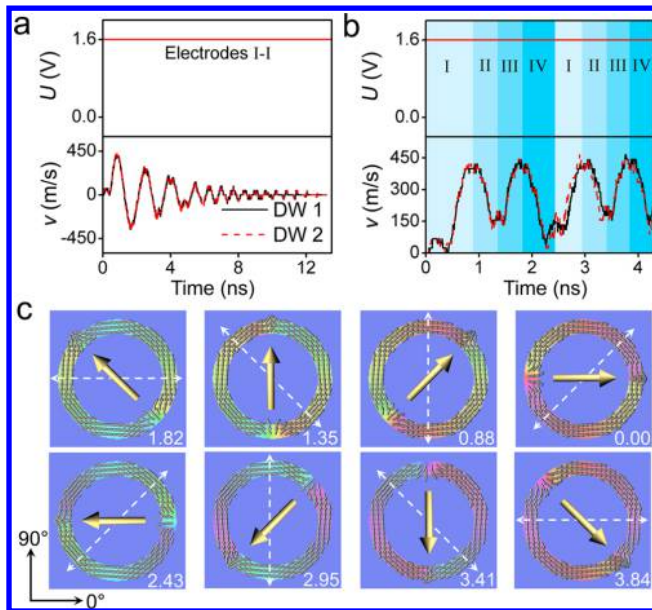
Figure 2. (a) Oscillatory and (b) unidirectional magnetic domain-wall (DW) motion in the amorphous CoFeB ring driven by a static voltage applied to electrodes I–I and by stepping control of all four pairs of top electrodes, respectively. (c) Snapshots (time unit in nanoseconds on the bottom right) of the magnetization distributions (top view). The solid arrows indicate the orientations of the effective magnetization vector. The dashed (double-headed) arrows indicate the orientations of the equivalent uniaxial tensile piezostrains.

the two magnetic domain-walls propagate synchronously (because of the identical values of their instantaneous velocities) in an oscillatory manner (because of the positive and negative velocities, also see Supplementary Video S1).

Further, Figure 2b shows that unidirectional (instantaneous velocities are all positive) magnetic domain-wall motion can be achieved by applying nanosecond-long, unipolar voltage pulses consecutively to the electrodes I–I, II–II, III–III, and IV–IV (see the top panel for the timing control). Note that applying 1.1 V to electrodes II–II, III–III, and IV–IV produces electric field distributions and surface piezostrain distributions that are symmetric to those shown in Figure 1d and e, because the dielectric and piezoelectric responses are isotropic in the plane for an out-of-plane poled polycrystalline PZT with ∞m symmetry. These unipolar voltages effectively prevent the depoling of the PZT disk and suppress ferroelectric domain-wall motion. As shown in Figure 2c, when the domain-walls move to 45° and 225° within 0.88 ns at their peak velocities (cf. Figure 2b), the 1.1 V voltage applied to the electrodes I–I is shut off. Then another 1.1 V is applied to electrodes II–II. Piezostrain of the same magnitude (i.e., 0.0766%, represented by the double-headed dashed arrow) drives the domain-walls to 90° and 270°. After voltage on electrodes II–II is shut off at 1.35 ns, another 1.1 V is applied to electrodes III–III until 1.82 ns. The domain-walls keep moving to 135° and 315° during this process. Further application of a 1.1 V to electrodes IV–IV continues to drive the domain-walls to 180° and 360° at 2.43 ns. Repeating these voltage sequences produces a full 360° domain-wall cycle (see full process in Supplementary Video S2). The average domain-wall velocity for this operation is approximately 255 m/s. Supplementary Figure S2 shows two examples of possible device architectures that utilize such voltage-driven unidirectional domain-wall motion.

Discussions. Here, the piezostrain-mediated voltage-driven unidirectional magnetic domain-wall motion is based on four coupled kinetic processes: (1) creation/release of electric field upon turning on/off voltages with RC (resistance–capacitance) delay; (2) rise/release of local piezostrains within the central surface region of the PZT disk under pulse voltage drive; (3) strain transfer across the interface; (4) strain-driven magnetic domain-wall motion in the CoFeB ring. Accordingly, the duration of voltage pulse must be sufficiently long to allow the completion of these processes. Taken together, a voltage-driven average magnetic wall velocity of about 170 m/s is predicted (see analyses in Methods) under a piezostrain of 0.0766%.

During one 180° magnetic domain-wall cycle around the ring, the energy consumption and heat dissipation from the PZT disk are approximately 4 fJ and 0.2 fJ, respectively (see details of estimation in Methods). The magnetic domain-wall propagation also dissipates a certain amount of heat as discussed below.

To quantify the heat dissipation during magnetic wall propagation, we consider a magnetic domain-wall as an effective particle with mass m^*.[31] Building on that, the oscillatory domain-wall propagation under a static voltage (strain) is analogous to a ball rolling down (see schematics in Figure 3a). In this case, the elastic energy density difference between 0° (180°) and 45° (225°) (see Figure 1f) corresponds to the gravitational energy difference between the high and low positions, and the magnetic damping that slows down wall propagation corresponds to the mechanical friction. Therefore, by analogy with the conversion between the gravitational potential energy and the kinetic energy, one has,
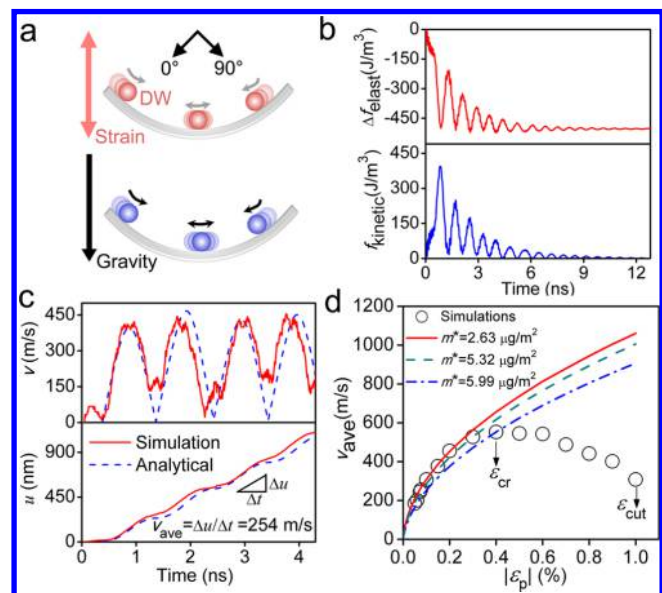

Figure 3. (a) Schematics of the oscillatory motion of the domain-walls around the strain axis by analogy to a ball rolling down under gravity. (b) Time-dependent changes in the instantaneous elastic energy density f_{elast} (top panel) and the kinetic energy density $f_{kinetic}$ (bottom panel) corresponding to the oscillatory motion. (c) Instantaneous velocities (top panel) and corresponding displacement (bottom panel) during one 360° magnetic domain-wall circuit predicted from both phase-field simulations and analytical modeling. (d) Average domain-wall velocity v_{ave} during one 360° cycle of unidirectional magnetic domain-wall motion as a function of the magnitude of the piezostrain $|\varepsilon_p|$ from phase-field simulations (open circles) and analytical model (lines) under different values of effective domain-wall mass (m^*).

$$\frac{1}{2}m^*v(t)^2 + \beta \int_0^t v(t)^2 dt = F_{elast}(t=0) - F_{elast}(t) \tag{1}$$

where the elastic energy difference on the right represents an energy reservoir for the domain-wall motion. The first term on the left represents the effective kinetic energy, and the second term describes the heat dissipation where β is the viscous damping parameter of the wall. For illustration, the top panel of Figure 3b shows the time-dependent changes in the elastic energy density $\Delta f_{elast}(t) = [f_{elast}(t) - f_{elast}(t=0)]$ under a static 1.1-V-voltage (and hence the strain of 0.0766%) applied to electrodes I−I, while changes in the effective kinetic energy density ($f_{kinetic}$) are shown in the bottom panel of Figure 3b. Equation 1 suggests an experimental approach to determine the effective magnetic domain-wall mass m^* by monitoring the instantaneous magnetic domain-wall velocity[32,33] $v(t)$ upon applying a static strain to a magnetic ring. Here, based on the calculated $v(t)$, the value of m^* is determined to be approximately 2.63 $\mu g/m^2$, which is smaller than the m^* of the in-plane transverse domain-walls in a $Ni_{81}Fe_{19}$ ring (about 21 $\mu g/m^2$, ref 31). This is mainly due to the smaller Gilbert damping factor (α_G, proportional to β) in the amorphous CoFeB ($\alpha_G = 0.0042$, ref 25), compared to 0.01 in polycrystalline $Ni_{81}Fe_{19}$.[34]

Based on the calculated β ($\approx 7.28 \times 10^{-16}$ (J·s)/m²) and the simulated $v(t)$ (see the solid line in the top panel of Figure 3c for the average $v(t)$ of the two magnetic domain-walls), the heat dissipation caused by magnetic domain-wall motion (the second term in in eq 1) is approximately 0.00026 fJ during one 180° circuit, which is negligible compared to heat dissipation from the piezoelectric actuator (~0.2 fJ).

By taking the time derivative on both sides of eq 1, the equation of motion for the magnetic domain-wall can be derived as (see details in Supplementary Figure S3 and Supplementary Note S1),

$$m^*\frac{dv(t)}{dt} + \beta v(t) = -\frac{3k^2\lambda_s V_{ring}}{2r}\frac{Y}{1+\nu_0}(1-\eta)$$
$$\varepsilon_p \sin(2\theta(v(t))) \tag{2}$$

where k is the magnitude of the normalized effective magnetization vector m_{eff}; λ_s is the saturation magnetostriction coefficient, V_{ring} is the volume of the ring, and r is the radius (taken as 175 nm); Y and ν_0 are the Young's modulus (~162 GPa, ref 35) and Poisson's ratio (~0.3, ref 24) of the amorphous CoFeB, respectively; θ is the angle between the rotating m_{eff} and the axis of uniaxial piezostrain (ε_p); η represents the degree of strain relaxation (~30%). Equation 2 can be utilized to predict the oscillating $v(t)$ during the dynamic-piezostrain-driven unidirectional magnetic domain-wall motion (see details in Supplementary Note S1) and thereby predict the average magnetic domain-wall velocity (v_{ave}). Taking $\varepsilon_p = 0.0766\%$, for instance, the curves of $v(t)$ and the corresponding displacements, $u(t)$ [$= \int v(t)dt$], calculated through eq 2 are compared with the simulated curves in Figure 3c. Note that, in the simulated curves, there exists an incubation delay at the initial stage (0−0.38 ns) during which there is no appreciable displacement. The duration of this period would be longer if the initial magnetic domain structure were more stable (see Supplementary Figure S4 and Note S2). This is reminiscent of the delay in magnetization switching in magnetic tunnel junctions driven by spin-transfer-torque.[36] Apart from this incubation delay, the curves obtained through eq 2 and

phase-field simulations are generally consistent, though there are also discrepancies in the minimum values of velocities and broadening/shifting of the peaks most likely due to magnetization inhomogeneity. Notably, the v_{ave} predicted through eq 2 and simulations (247 and 254 m/s, respectively) are quite close.

Figure 3d further shows the v_{ave} under various ε_p up to 1%. Experimentally a biaxial in-plane anisotropic piezostrain difference up to 0.5% has been observed in a piezoelectric PMN−PT single crystal.[30] As shown in Figure 3d, v_{ave} first increases, then decreases with increasing ε_p, and falls to zero when ε_p exceeds a cutoff value (ε_{cut}) of 1%. A peak velocity of about 553 m/s appears at a critical strain (ε_{cr}) of 0.4%. On the other hand, with the input values of m^* and β obtained when $\varepsilon_p = 0.0766\%$, the results calculated from the analytical theory (see the red line) agree quite well with the phase-field simulation results (symbols) when ε_p is below 0.2%. Below, we will discuss the reasons for the deviations arising under larger ε_p.

First, we attribute the deviations at $0.2\% < \varepsilon_p \leq 0.4\%$ to the enhanced structural instability of the magnetic domain-walls, which can be interpreted as the enhancement of the magnetic domain-wall mass. For illustration, after utilizing the updated input values of m^* (determined to be about 5.32 $\mu g/m^2$ and 5.99 $\mu g/m^2$ from the oscillating $v(t)$ on applying a static ε_p of 0.3% and 0.4%, respectively), the calculated v_{ave} is consistent with the simulation results (see the dashed and dashed dotted lines in Figure 3d). As a direct evidence for the enhanced structural instability, at $\varepsilon_p = 0.3\%$ and 0.4%, the in-plane magnetization vectors inside the domains walls experience appreciable out-of-plane excursion when the domain-walls propagate (see Supplementary Figure S5a and Note S3). Second, the onset of negative strain-controlled magnetic domain-wall mobility (i.e., $dv_{ave}/d\varepsilon_p$) when ε_p exceeds 0.4% is caused by the breakdown of the synchronous motion of the two domain-walls. This asynchronous motion is evidenced by the marked difference in the phases of the instantaneous velocities $v(t)$ of the two magnetic domain-walls (Supplementary Figure S5b) and the formation of metastable asymmetric onion domains[37] (image on the left of Supplementary Figure S5c) and is directly shown in Supplementary Video S3; this asynchronous motion is a result of the enhanced structural instability of not only the magnetic domain-walls but also the magnetic domains (Supplementary Figure S5d and Note S3). For such asynchronous magnetic domain-wall motion, eq 2 is no longer applicable. Third, for ε_p larger than 1%, the torque provided by the strain would be too large, such that the onion-type magnetic domain structure and the transverse domain-wall structure cannot be maintained (image on the right of Supplementary Figure S5c), and hence the 360° domain-wall motion is cut off.

Thus, it is important to obtain a domain-wall with high structural stability in the magnetic ring, such that larger piezostrains can be applied to increase the wall velocity without drastically changing the wall structure. This paradigm of increasing wall velocity is similar to that in current-driven magnetic domain-wall motion.[10,12] With this in mind, a stability diagram containing six different domain-wall structures as a function of the thickness and the outer diameter of the magnetic ring is constructed. The solid circle in Figure 4a, indicating the present dimensions of 300 nm × 400 nm × 5 nm, is in the central region of the in-plane transverse domain-wall (phase (i). Hence the wall structure should be more stable than those in the vicinity of a phase boundary (see Figure 4a).
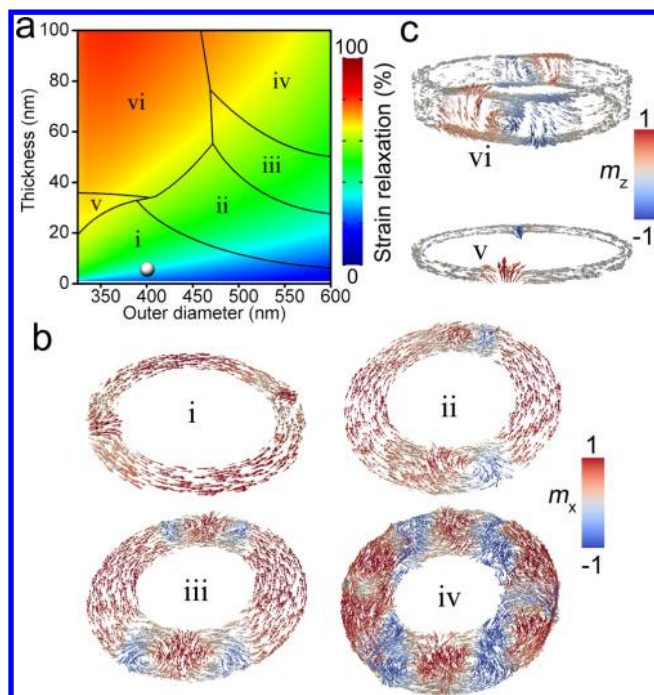
Figure 4. (a) Domain-wall structure stability diagram as a function of the thickness and the outer diameter of the CoFeB ring. The background color shows the degree of strain relaxation at each dimension. (b–c) Three-dimensional illustration of the typical domain-wall structures for dimensions of (from i to vi) 300 nm × 400 nm × 5 nm, 300 nm × 500 nm × 30 nm, 300 nm × 550 nm × 45 nm, 300 nm × 550 nm × 70 nm, 300 nm × 325 nm × 30 nm, and 300 nm × 350 nm × 80 nm, respectively. The inner diameter of the ring is fixed as 300 nm.

In addition to high structural stability, a low degree of strain relaxation (η, represented by the background color) is also desirable for obtaining high strain-mediated voltage-driven magnetic domain-wall velocity.

It can also be seen from Figure 4a that the in-plane transverse domain-wall structure (phase i) is favored in thin and narrow rings and would gradually transform into single, double, and multiple vortex domain-walls (phases ii, iii, and iv, respectively) when the ring becomes wider and thicker. Figure 4b illustrates the representative structures for these in-plane domain-walls. Such a size-dependent transverse to vortex domain-wall transformation has been experimentally observed in ring-shaped Co[38] and $Ni_{80}Fe_{20}$ magnets.[39] Our simulations also suggest a transformation from an in-plane transverse wall to an out-of-plane transverse wall (phase v), then to an out-of-plane vortex wall (phase vi) in relatively narrow and thick magnetic rings, as shown in Figure 4c. Among all six domain-wall structures, the in-plane transverse wall exhibits the highest mobility in response to strain (see Supplementary Figure S6 and Note S4).

In summary, we have demonstrated fast and unidirectional voltage-driven magnetic domain-wall motion in a rough-edged magnetic ring by controlling the magnetic wall dynamics using fast piezostrains. The simulation results suggest a high average domain-wall velocity up to 550 m/s, which is comparable to that through spin-torque-mediated current-driven magnetic domain-wall motion.[11,12] However, the heat dissipation (~0.2 fJ per 180° magnetic domain-wall circuit around the ring) is approximately 3 orders of magnitude smaller (~0.2 pJ and above in current-driven cases, see Supplementary Note S5).

Moreover, the energy consumption (~4 fJ) is ultralow. Further enhancement of magnetic domain-wall velocity and further reduction of energy dissipation/consumption is possible by optimizing the structure design. From a fundamental perspective, the simulation results have revealed the dynamics of such strain-mediated voltage-driven unidirectional magnetic domain-wall motion (Figure 3d), the feature of which is completely different from the features of magnetic domain-wall dynamics controlled by currents or magnetic field.[40] An analytical theory has been developed to understand the simulation results on the strain-controlled magnetic domain-wall dynamics at small strains. This theory also suggests a new method of extracting the effective mass of a magnetic domain-wall by experiments.

Overall, this work shows how to achieve fast and unidirectional magnetic domain-wall motion driven by an applied voltage. The maximum average domain-wall velocity shown in this work (about 550 m/s) is over five times higher than that of the voltage-driven bidirectional magnetic domain-wall motion (<100 m/s) demonstrated computationally in a straight magnetic nanowire (with hypothetical material parameters) covered by PZT film.[13] In contrast to one singular previous report of voltage-driven unidirectional magnetic domain-wall motion, this work does not require ferroelastic domains that possess a specific pattern and width to elastically pin the magnetic domains.[41] Furthermore, the maximum voltage-driven magnetic domain-wall velocity in that report[41] is below 10^{-5} m/s, 7 orders of magnitude smaller than 550 m/s. It is worth noting that such fast and unidirectional voltage-driven magnetic domain-wall motion can also be realized by employing other electrode designs that permit the generation of a uniaxial piezostrain on the surface of the PZT disk, in addition to the electrode design shown in Figure 1a. A wide variety of piezoelectric and ferroelastic materials are potential candidates to be used for the proposed device although materials with high converse piezoelectric responses are preferable. Large piezostrains are important to overcoming randomly distributed local pinning potentials from the rough edges (see Figure 1b and Figure 2c) and other possible defects due to patterning imperfections. Apart from the ring-shaped nanowire used for demonstration, the basic principle in this work is also applicable to other curved nanowires.

Methods. *Phase-Field Simulations.* The whole simulation zone is discretized into a three-dimensional array of cuboid cells of $150\Delta x \times 150\Delta y \times 20\Delta z$. Three phase-field order parameters $\mathbf{O_p}$, $\mathbf{O_m}$, $\mathbf{O_a}$ are employed to describe the piezoelectric nanoisland, the patterned magnetic ring, and the air, where $(\mathbf{O_p}, \mathbf{O_m}, \mathbf{O_a})$ = (1,0,0), (0,1,0), and (0,0,1), respectively. Specifically, the bottom cells of $150\Delta x \times 150\Delta y \times 10\Delta z$ are designated as the piezoelectric phase that provides uniaxial or biaxial in-plane piezostrains. The magnetic ring occupies a fraction of the overlaid cells of $150\Delta x \times 150\Delta y \times 5\Delta z$ in such a way that the spatial distribution of O_m obeys a shape function with a diffuse interface between the ring and the air, i.e., $O_m = 0.5[\tanh[8(\mathbf{r_0} - r_1)] - \tanh[8(\mathbf{r_0} - r_2)]]$, wherein r_1 and r_2 denote the inner and outer radii of the ring, and $\mathbf{r_0}$ is the distance between the center of the ring and a given cell. This shape function allows us to introduce edge roughness (about 4 nm on average in this work) that would appear in experiments due to patterning imperfections. The topmost cells of $150\Delta x \times 150\Delta y \times 5\Delta z$ represent air, which is introduced to accommodate the magnetic stray fields and to establish stress-free surfaces for the ring such that mechanical relaxation

occurs upon applying strains. The latter is achieved by setting the elastic constants of the air to zero when calculating the total elastic energy through a spectral iterative perturbation method.[42] The size of each cell is taken as $\Delta x \times \Delta y \times \Delta z = 3$ nm $\times$ 3 nm $\times$ 1 nm in real space to describe a whole system of 450 nm $\times$ 450 nm $\times$ 20 nm (with $r_1 = 150$ nm and $r_2 = 200$ nm). By varying the number of the cells, the cell size, and the ratio of r_1 to r_2, magnetic rings of different sizes (Figure 4) can be considered.

Within the magnetic ring, the spatial distribution of local magnetization vector $\mathbf{M} = M_s(\mathbf{m}_x, \mathbf{m}_y, \mathbf{m}_z)$ represent the magnetic domain and domain-walls, where M_s is the saturation magnetization ($\sim 1.2 \times 10^6$ A/m for amorphous $Co_{40}Fe_{40}B_{20}$, ref [43]). The equation of motion for magnetization follows the typical Landau–Lifshitz–Gilbert (LLG) form,

$$\frac{\partial \mathbf{m}}{\partial t} = -\gamma_0(\mathbf{m} \times \mathbf{H}_{eff}) + \alpha_G\left(\mathbf{m} \times \frac{\partial \mathbf{m}}{\partial t}\right) \tag{3}$$

where the first term on the right is the precession torque that accounts for the gyrotropic motion of magnetization around the effective field $\mathbf{H}_{eff}$ with the prefactor γ_0 denoting the gyromagnetic ratio ($\sim 1.76 \times 10^{11}$ Hz/T, ref [44]), while the second term is the damping torque. $\mathbf{H}_{eff}$ is calculated as $-(1/\mu_0 M_s)(\delta F_{tot}/\delta \mathbf{m})$, where μ_0 is the vacuum permeability and F_{tot} is the total magnetic free energy of the whole system consisting of the amorphous nanomagnet, written as,

$$F_{tot} = \int [A|\nabla \mathbf{m}|^2 - 0.5\mu_0 M_s(\mathbf{H}_d \cdot \mathbf{m}) + 0.5(\boldsymbol{\varepsilon} \cdot \mathbf{c} \cdot \boldsymbol{\varepsilon})] dV \tag{4}$$

where the terms inside the volume integral describe the exchange energy density, stray field energy density, and elastic energy density, respectively; A is the exchange constant of the amorphous $Co_{40}Fe_{40}B_{20}$, taken as 1.5×10^{-11} A/m from ref [25]; $\mathbf{H}_d$ is the stray field; $\mathbf{c}$ is the elastic stiffness tensor that is spatially variant in the system; $\boldsymbol{\varepsilon}$ is the elastic strain tensor that can be expanded as $\boldsymbol{\varepsilon} = \boldsymbol{\varepsilon}^{hom} + \boldsymbol{\varepsilon}^{het} - \boldsymbol{\varepsilon}^0$, and is obtained by solving mechanical equilibrium equation ($\nabla \cdot (\mathbf{c}\boldsymbol{\varepsilon}) = 0$) Here the homogeneous strain $\boldsymbol{\varepsilon}^{hom}$ corresponds to the actual deformation arising from the transfer of in-plane piezostrains $\boldsymbol{\varepsilon}_p$ across the magnetic-piezoelectric interface; $\boldsymbol{\varepsilon}^{het}$ is the heterogeneous strain whose volume average is zero; the eigenstrain $\boldsymbol{\varepsilon}^0$ corresponds to the magnetostrictive deformation under stress-free condition, with $\varepsilon_{ij}^0 = 1.5\lambda_s(m_i m_j - 1/3)$ and $1.5\lambda_s m_i m_j$ for $i = j$ and $i \neq j$, respectively. A saturation magnetostriction λ_s of about 31 ppm is taken from ref [24]. Details of calculating $\mathbf{H}_d$ and $\boldsymbol{\varepsilon}$ for such finite-size patterned magnetic nanostructures have been given in ref [42]. In the present phase-field model with coupled micromagnetics and elasticity, strain state is constantly recalculated during the temporal evolution of local magnetization, while in conventional micromagnetic simulations, strains are fed into eq 3 as an effective magnetic field in one direction.

Finite-Element Analyses. The finite-element model is implemented in COMSOL Multiphysics commercial software. The equilibrium distributions of electric field ($\mathbf{E}$) and elastic strains ($\boldsymbol{\varepsilon}$) are obtained by solving coupled electrostatic equilibrium equation ($\nabla \cdot \mathbf{D} = 0$) and mechanical equilibrium equation ($\nabla \cdot \boldsymbol{\sigma} = 0$), where the electric displacement ($\mathbf{D}$) and stress ($\boldsymbol{\sigma}$) are expressed based on the coupled constitutive equations,

$$D = e\varepsilon + \varepsilon_0 \varepsilon_r E$$

$$\sigma = c_E \varepsilon - e^T E \tag{5}$$

where $\mathbf{e}^T$ is the transpose of the piezoelectric coefficient measured under constant temperature; ε_0 is the vacuum permittivity, and $\boldsymbol{\varepsilon}_r$ is the relative permittivity; $\mathbf{c}_E$ denotes the elastic stiffness coefficient measured under constant electric fields. The electrostatic and mechanical equilibrium boundary conditions are solved are solved using MUMPS (MUltifrontal Massively Parallel Sparse direct Solver). Free tetrahedral meshes are built with cubic and quadratic shape functions to solve mechanical and electrostatic equilibrium equations, respectively. Top surfaces of a soft PZT ceramic and the electrodes are stress-free. The PZT is fixed everywhere else (i.e., with zero mechanical displacement), which can be achieved experimentally by depositing thick and stiff Al_2O_3 layers[45] on the lateral sides of the nanostructure. A constant gate voltage of 1.1 V is applied to a single pair of top electrodes (e.g., I–I), while the other inactive top electrodes are kept under open-circuit condition. The bottom electrode is electrically grounded at 0 V. Values of the full matrices of the $\mathbf{e}$, $\boldsymbol{\varepsilon}_r$, and $\mathbf{c}_E$ can be found in Supplementary Note S6.

The mechanical resonance frequency (f_r) of the proposed design was determined through the frequency analysis module in COMSOL Multiphysics. An alternating voltage with a 1.1-V-amplitude and a frequency varying from 1 to 5 GHz is applied to electrodes I–I. The mechanical displacement of a point at the electrode tip is plotted as a function of the voltage frequency. The f_r, at which this displacement achieves maximum, is approximately 2.4 GHz.

Estimating the Time Required by the Different Kinetic Processes. Here the RC delay ($t_{RC} \approx R \times C$) can be as small as about 0.15 ps. This delay includes a typical resistance (R) of about 100 Ω (ref [46]), and a capacitance (C) approximately 0.0015 pF according to $C \approx \varepsilon_0 \varepsilon_r S/d$, where S (~ 0.2 μm^2) is the area of a pair of top electrodes and d is the thickness (400 nm). The minimum rise/release time of the homogeneous piezostrain (t_p) of the entire PZT disk can be estimated based on $t_p \approx 1/(3f_r)$[47] and is approximately 0.14 ns given $f_r \approx 2.4$ GHz. The rise of local piezostrain within the central surface region could be faster. Such local piezostrains propagate across the interface in the form of mechanical waves,[48] and can spread over the CoFeB ring within about 1 ps. This duration is estimated by dividing the ring thickness by the speed of sound (v_s, approximately 4500 m/s) in the amorphous CoFeB. The latter is calculated through Newton–Laplace equation, $v_s = (Y/\rho)^{1/2}$, by taking a density (ρ) of 8 g/cm^3. Further, the time required by the strain-driven magnetic domain-wall motion averages 0.54 ns during each stage (see Figure 2b). Taken together, only the rise/release time of piezostrains (process 2) is comparable to the time required by the magnetic changes (process 4) and hence may slow down the speed of voltage-driven magnetic domain-wall motion. As a conservative estimate, by adding 0.28 ns in each one of eight stages to make sure the piezostrain reaches its nominal value and decreases to zero, the voltage-driven average magnetic domain-wall velocity still remains as high as 168 m/s.

Estimating the Energy Consumption and Dissipation. The energy consumption (E_{con}) is approximately 3.63 fJ based on $E_{con} = n0.5CU^2$, where n is the number of charging–discharging cycles ($n = 4$ per 180° domain-wall circuit). The average power dissipation (P) by the PZT can be calculated based on $P \approx$

$n0.25\pi f C \tan\delta\, U^2$,[47] where f (≈ 0.46 GHz) and U (1.1 V) are frequency and magnitude of the unipolar voltage, respectively, and $\tan\delta$ indicates the low signal dielectric loss of the polycrystalline PZT (approximately 0.03, ref [49]). The total heat dissipation by the PZT per $180°$ domain-wall circuit can therefore be calculated to be about 0.17 fJ. The actual heat dissipation could be larger due to the field dependence of the loss tangent.[50,51] In practice, if this became too large, then a domain engineered piezoelectric or an electrostrictive material could be substituted for the PZT.

ASSOCIATED CONTENT

ⓈSupporting Information

The Supporting Information is available free of charge on the ACS Publications website at DOI: 10.1021/acs.nano-lett.5b05046.

> Additional results and discussions include supplementary Figure S1–S6, Note S1–S6, Video S1–S3, and references (PDF)

AUTHOR INFORMATION

Corresponding Authors
*E-mail: juh34@psu.edu (J.-M.H.).
*E-mail: lqc3@psu.edu (L.-Q.C.).

Author Contributions

J.-M.H. and T.Y. contributed equally to this work. J.-M.H. conceived the design. J.-M.H. and L.-Q.C. led the studies. J.-M.H. and T.Y. performed phase-field simulations and analytical calculations. K.M. performed finite-element analyses. X.C. contributed to the potential device designs in Supplemental Figure S2. S.L. performed finite-element analyses for Supplemental Figure S1b. J.-M.H. and L.-Q.C. wrote the manuscript, using substantial feedback from K.M., L.C., S.Z., S.T.-M., V.G., G.P.C., and C.-W.N. The authors declare no competing financial interest.

Notes

The authors declare no competing financial interest.

ACKNOWLEDGMENTS

REFERENCES

(1) Allwood, D. A.; Xiong, G.; Faulkner, C. C.; Atkinson, D.; Petit, D.; Cowburn, R. P. *Science* **2005**, *309* (5741), 1688−1692.

(2) Mattheis, R.; Diegel, M.; Hubner, U.; Halder, E. *IEEE Trans. Magn.* **2006**, *42* (10), 3297−3299.

(3) Parkin, S. S. P.; Hayashi, M.; Thomas, L. *Science* **2008**, *320* (5873), 190−194.

(4) Atkinson, D.; Allwood, D. A.; Xiong, G.; Cooke, M. D.; Faulkner, C. C.; Cowburn, R. P. *Nat. Mater.* **2003**, *2* (2), 85−87.

(5) Nakatani, Y.; Thiaville, A.; Miltat, J. *Nat. Mater.* **2003**, *2* (8), 521−523.

(6) Beach, G. S. D.; Nistor, C.; Knutson, C.; Tsoi, M.; Erskine, J. L. *Nat. Mater.* **2005**, *4* (10), 741−744.

(7) Yamaguchi, A.; Ono, T.; Nasu, S.; Miyake, K.; Mibu, K.; Shinjo, T. *Phys. Rev. Lett.* **2004**, *92* (7), 077205.

(8) Kläui, M.; Vaz, C. A. F.; Bland, J. A. C.; Wernsdorfer, W.; Faini, G.; Cambril, E.; Heyderman, L. J.; Nolting, F.; Rüdiger, U. *Phys. Rev. Lett.* **2005**, *94* (10), 106601.

(9) Chanthbouala, A.; Matsumoto, R.; Grollier, J.; Cros, V.; Anane, A.; Fert, A.; Khvalkovskiy, A. V.; Zvezdin, K. A.; Nishimura, K.; Nagamine, Y.; Maehara, H.; Tsunekawa, K.; Fukushima, A.; Yuasa, S. *Nat. Phys.* **2011**, *7* (8), 626−630.

(10) Miron, I. M.; Moore, T.; Szambolics, H.; Buda-Prejbeanu, L. D.; Auffret, S.; Rodmacq, B.; Pizzini, S.; Vogel, J.; Bonfim, M.; Schuhl, A.; Gaudin, G. *Nat. Mater.* **2011**, *10* (6), 419−423.

(11) Metaxas, P. J.; Sampaio, J.; Chanthbouala, A.; Matsumoto, R.; Anane, A.; Fert, A.; Zvezdin, K. A.; Yakushiji, K.; Kubota, H.; Fukushima, A.; Yuasa, S.; Nishimura, K.; Nagamine, Y.; Maehara, H.; Tsunekawa, K.; Cros, V.; Grollier, J. *Sci. Rep.* **2013**, *3*, 1829.

(12) Yang, S.-H.; Ryu, K.-S.; Parkin, S. *Nat. Nanotechnol.* **2015**, *10* (3), 221−226.

(13) Dean, J.; Bryan, M. T.; Schrefl, T.; Allwood, D. A. *J. Appl. Phys.* **2011**, *109* (2), 023915.

(14) Bauer, U.; Emori, S.; Beach, G. S. D. *Appl. Phys. Lett.* **2012**, *100* (19), 192408.

(15) Chiba, D.; Kawaguchi, M.; Fukami, S.; Ishiwata, N.; Shimamura, K.; Kobayashi, K.; Ono, T. *Nat. Commun.* **2012**, *3*, 888.

(16) Schellekens, A. J.; van den Brink, A.; Franken, J. H.; Swagten, H. J. M.; Koopmans, B. *Nat. Commun.* **2012**, *3*, 847.

(17) Bernand-Mantel, A.; Herrera-Diez, L.; Ranno, L.; Pizzini, S.; Vogel, J.; Givord, D.; Auffret, S.; Boulle, O.; Miron, I. M.; Gaudin, G. *Appl. Phys. Lett.* **2013**, *102* (12), 122406.

(18) Franken, J. H.; Yin, Y.; Schellekens, A. J.; van den Brink, A.; Swagten, H. J. M.; Koopmans, B. *Appl. Phys. Lett.* **2013**, *103* (10), 102411.

(19) Bauer, U.; Yao, L.; Tan, A. J.; Agrawal, P.; Emori, S.; Tuller, H. L.; van Dijken, S.; Beach, G. S. D. *Nat. Mater.* **2014**, *14*, 174−181.

(20) Mikheev, E.; Stolichnov, I.; De Ranieri, E.; Wunderlich, J.; Trodahl, H. J.; Rushforth, A. W.; Riester, S. W. E.; Campion, R. P.; Edmonds, K. W.; Gallagher, B. L.; Setter, N. *Phys. Rev. B: Condens. Matter Mater. Phys.* **2012**, *86* (23), 235130.

(21) Huang, Z.; Stolichnov, I.; Bernand-Mantel, A.; Borrel, J.; Auffret, S.; Gaudin, G.; Boulle, O.; Pizzini, S.; Ranno, L.; Herrera Diez, L.; Setter, N. *Appl. Phys. Lett.* **2013**, *103* (22), 222902.

(22) Lei, N.; Devolder, T.; Agnus, G.; Aubert, P.; Daniel, L.; Kim, J.-V.; Zhao, W.; Trypiniotis, T.; Cowburn, R. P.; Chappert, C.; Ravelosona, D.; Lecoeur, P. *Nat. Commun.* **2013**, *4*, 1378.

(23) De Ranieri, E.; Roy, P. E.; Fang, D.; Vehstedt, E. K.; Irvine, A. C.; Heiss, D.; Casiraghi, A.; Campion, R. P.; Gallagher, B. L.; Jungwirth, T.; Wunderlich, J. *Nat. Mater.* **2013**, *12* (9), 808−814.

(24) Wang, D.; Nordman, C.; Qian, Z.; Daughton, J. M.; Myers, J. *J. Appl. Phys.* **2005**, *97* (10), 10C906.

(25) Conca, A.; Greser, J.; Sebastian, T.; Klingler, S.; Obry, B.; Leven, B.; Hillebrands, B. *J. Appl. Phys.* **2013**, *113* (21), 213909.

(26) Rothman, J.; Kläui, M.; Lopez-Diaz, L.; Vaz, C. A. F.; Bleloch, A.; Bland, J. A. C.; Cui, Z.; Speaks, R. *Phys. Rev. Lett.* **2001**, *86* (6), 1098.

(27) Cui, J.; Hockel, J. L.; Nordeen, P. K.; Pisani, D. M.; Liang, C.-y.; Carman, G. P.; Lynch, C. S. *Appl. Phys. Lett.* **2013**, *103* (23), 232905.

(28) Moazzami, R.; Hu, C.; Shepherd, W. H. *IEEE Trans. Electron Devices* **1992**, *39* (9), 2044−2049.

(29) Liang, C.-Y.; Keller, S. M.; Sepulveda, A. E.; Sun, W.-Y.; Cui, J.; Lynch, C. S.; Carman, G. P. *J. Appl. Phys.* **2014**, *116* (12), 123909.

(30) Sohn, H.; Nowakowski, M. E.; Liang, C.-y.; Hockel, J. L.; Wetzlar, K.; Keller, S.; McLellan, B. M.; Marcus, M. A.; Doran, A.; Young, A.; Kläui, M.; Carman, G. P.; Bokor, J.; Candler, R. N. *ACS Nano* **2015**, *9* (5), 4814−4826.

(31) Saitoh, E.; Miyajima, H.; Yamaoka, T.; Tatara, G. *Nature* **2004**, *432* (7014), 203−206.

(32) Hayashi, M.; Thomas, L.; Rettner, C.; Moriya, R.; Parkin, S. S. P. *Nat. Phys.* **2007**, *3* (1), 21−25.

(33) Bisig, A.; Stärk, M.; Mawass, M.-A.; Moutafis, C.; Rhensius, J.; Heidler, J.; Büttner, F.; Noske, M.; Weigand, M.; Eisebitt, S.; Tyliszczak, T.; Van Waeyenberge, B.; Stoll, H.; Schütz, G.; Kläui, M. *Nat. Commun.* **2013**, *4*, 2328.

(34) Ingvarsson, S.; Ritchie, L.; Liu, X. Y.; Xiao, G.; Slonczewski, J. C.; Trouilloud, P. L.; Koch, R. H. *Phys. Rev. B: Condens. Matter Mater. Phys.* **2002**, *66* (21), 214416.

(35) Hindmarch, A. T.; Rushforth, A. W.; Campion, R. P.; Marrows, C. H.; Gallagher, B. L. *Phys. Rev. B: Condens. Matter Mater. Phys.* **2011**, *83* (21), 212404.

(36) Devolder, T.; Hayakawa, J.; Ito, K.; Takahashi, H.; Ikeda, S.; Crozat, P.; Zerounian, N.; Kim, J.-V.; Chappert, C.; Ohno, H. *Phys. Rev. Lett.* **2008**, *100* (5), 057206.

(37) Castaño, F. J.; Ross, C. A.; Frandsen, C.; Eilez, A.; Gil, D.; Smith, H. I.; Redjdal, M.; Humphrey, F. B. *Phys. Rev. B: Condens. Matter Mater. Phys.* **2003**, *67* (18), 184425.

(38) Klaui, M.; Vaz, C. A. F.; Bland, J. A. C.; Heyderman, L. J.; Nolting, F.; Pavlovska, A.; Bauer, E.; Cherifi, S.; Heun, S.; Locatelli, A. *Appl. Phys. Lett.* **2004**, *85* (23), 5637.

(39) Roy, P.; Lee, J.; Trypiniotis, T.; Anderson, D.; Jones, G.; Tse, D.; Barnes, C. *Phys. Rev. B: Condens. Matter Mater. Phys.* **2009**, *79* (6), 060407.

(40) Mougin, A.; Cormier, M.; Adam, J. P.; Metaxas, P. J.; Ferré, J. *Europhys. Lett.* **2007**, *78* (5), 57007.

(41) Franke, K. J. A.; Van de Wiele, B.; Shirahata, Y.; Hämäläinen, S. J.; Taniyama, T.; van Dijken, S. *Phys. Rev. X* **2015**, *5* (1), 011010.

(42) Hu, J.-M.; Yang, T.; Wang, J.; Huang, H.; Zhang, J.; Chen, L.-Q.; Nan, C.-W. *Nano Lett.* **2015**, *15* (1), 616−622.

(43) Li, P.; Chen, A.; Li, D.; Zhao, Y.; Zhang, S.; Yang, L.; Liu, Y.; Zhu, M.; Zhang, H.; Han, X. *Adv. Mater.* **2014**, *26* (25), 4320−5.

(44) Liu, L.; Pai, C.-F.; Li, Y.; Tseng, H. W.; Ralph, D. C.; Buhrman, R. A. *Science* **2012**, *336* (6081), 555−558.

(45) Ikeda, S.; Miura, K.; Yamamoto, H.; Mizunuma, K.; Gan, H. D.; Endo, M.; Kanai, S.; Hayakawa, J.; Matsukura, F.; Ohno, H. *Nat. Mater.* **2010**, *9* (9), 721−724.

(46) Fashami, M. S.; Roy, K.; Atulasimha, J.; Bandyopadhyay, S. *Nanotechnology* **2011**, *22* (15), 155201.

(47) http://www.piceramic.com/piezo-technology/properties-piezo-actuators/.

(48) Schröder, K. *J. Appl. Phys.* **1982**, *53* (3), 2759−2761.

(49) Ledermann, N.; Muralt, P.; Baborowski, J.; Gentil, S.; Mukati, K.; Cantoni, M.; Seifert, A.; Setter, N. *Sens. Actuators, A* **2003**, *105* (2), 162−170.

(50) Pramanick, A.; Damjanovic, D.; Nino, J. C.; Jones, J. L. *J. Am. Ceram. Soc.* **2009**, *92* (10), 2291−2299.

(51) Bassiri-Gharb, N.; Fujii, I.; Hong, E.; Trolier-McKinstry, S.; Taylor, D.; Damjanovic, D. *J. Electroceram.* **2007**, *19* (1), 49−67.